[12] SICK Inc., LMS/LMI Telegram Listing, v. 05.00, p. 98.

[13] D. Nitzan *et al.*, "The measurement and use of registered reflectance and range data in scene analysis," *Proc. IEEE*, vol. 65, pp. 206–220, Feb. 1977.

[14] M. Hebert and E. Krotkov, "3D measurements from imaging laser radars: How good are they?," *Image Vis. Computing*, vol. 10, no. 3, pp. 170–178, 1992.

[15] C. F. Olson, "Adaptive-scale filtering and featuring detection using range data," *IEEE Trans. Pattern Anal. Machine Intell.*, vol. 22, pp. 983–991, Sept. 2000.

[16] A. K. Jain, *Fundamentals of Digital Image Processing*. Englewood Cliffs, NJ: Prentice-Hall, 1989.

[17] P. Perona and J. Malik, "Scale-space and edge detection using anisotropic diffusion," *IEEE Trans. Pattern Anal. Machine Intell.*, vol. 12, pp. 629–639, July 1990.

[18] D. R. K. Brownrigg, "The weighted median filter," *Commun. ACM*, vol. 27, no. 8, pp. 807–818, 1984.

[19] S. Ko and S. Lee, "Center weighted median filters and their applications to image enhancement," *IEEE Trans. Circuits Syst.*, vol. 38, pp. 984–993, Sept. 1991.

[20] H. Lin and A. N. Willson, Jr., "Median filters with adaptive length," *IEEE Trans. Circuits Syst.*, vol. 35, pp. 675–690, June 1988.

[21] T. Chen and H. R. Wu, "Application of partition-based median type filters for suppressing noise in images," *IEEE Trans. Image Processing*, vol. 10, pp. 829–836, June 2001.

[22] H. Eng and K. Ma, "Noise adaptive soft-switching median filter," *IEEE Trans. Image Processing*, vol. 10, pp. 242–251, Feb. 2001.

[23] T. Chen, K. Ma, and L. Chen, "Tri-state median filter for image denoising," *IEEE Trans. Image Processing*, vol. 8, pp. 1834–1838, Dec. 1999.

[24] M. D. Adams and P. J. Probert, "The interpretation of phase and intensity data from AMCW light detection sensors for reliable ranging," *Int. J. Robot. Res.*, vol. 15, no. 5, pp. 441–458, 1996.

Online Terrain Parameter Estimation for Wheeled Mobile Robots With Application to Planetary Rovers

Karl Iagnemma, Shinwoo Kang, Hassan Shibly, and Steven Dubowsky

Abstract—Future planetary exploration missions will require wheeled mobile robots ("rovers") to traverse very rough terrain with limited human supervision. Wheel–terrain interaction plays a critical role in rough-terrain mobility. In this paper, an online estimation method that identifies key terrain parameters using on-board robot sensors is presented. These parameters can be used for traversability prediction or in a traction control algorithm to improve robot mobility and to plan safe action plans for autonomous systems. Terrain parameters are also valuable indicators of planetary surface soil composition. The algorithm relies on a simplified form of classical terramechanics equations and uses a linear-least squares method to compute terrain parameters in real time. Simulation and experimental results show that the terrain estimation algorithm can accurately and efficiently identify key terrain parameters for various soil types.

Index Terms—Mobile robots, planetary rovers, rough terrain, wheel–terrain interaction.

I. INTRODUCTION

Future planetary exploration missions will require rovers to perform challenging mobility tasks in rough terrain [1]–[4]. Proposed future mission objectives include traversal of several kilometers with a high degree of autonomy. To accomplish these objectives, future control and planning methods must consider the physical characteristics of the rover and its environment to fully utilize the rover's capabilities.

Wheel–terrain interaction plays a critical role in rough-terrain mobility [5]–[7]. For example, a robot traveling through loose sand has very different mobility characteristics than one moving across firm clay. It is important to estimate terrain physical parameters online, since this would allow a robot to predict its ability to safely traverse terrain [8]. It would also allow a robot to adapt its control and planning strategy to maximize wheel traction or minimize power consumption [9]. Finally, estimation of terrain parameters is an important scientific goal of planetary surface exploration missions [10]–[12].

Several researchers have studied terrain parameter estimation. Generally, these methods involve offline estimation using dedicated testing equipment [13], [14]. Parameter estimation for a legged system has been studied in [15]. This approach relies on feedback from an embedded multi-axis force sensor in the robot's leg and is not applicable to wheeled systems. Terrain parameter estimation for tracked vehicles has been proposed in [16]. This approach assumes a highly simplified "force coefficient" model of track–terrain interaction, which is not valid in deformable rough terrain.

Parameter estimation of Martian soil has been performed by the Viking landers and the Sojourner rover. The Viking landers used manipulator arms to conduct soil trenching experiments [10]. The Sojourner
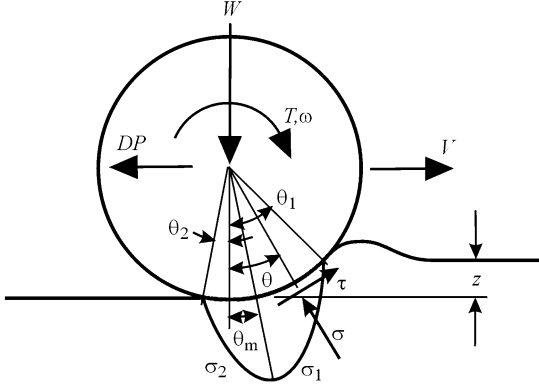
Fig. 1.   Free-body diagram of a rigid wheel on deformable terrain.

rover used the rover wheel as a trenching device to identify soil cohesion and internal friction angle [11]. Both missions used visual cues and offline (earth-based) analysis techniques to compute soil parameters. Earth-based analysis requires lengthy communication time delays that reduce rover efficiency and limit its autonomy.

In this paper, a method for online estimation of two key terrain parameters, cohesion and internal friction angle, is presented. The particular application of planetary exploration is addressed. The algorithm relies on a simplified form of classical terramechanics equations and uses a linear-least squares estimator to compute terrain parameters in real time. The method is computationally efficient and thus suitable for implementation on a rover with limited computational resources. Also, the method uses sensors that are likely to be part of future planetary rover systems and thus does not add to system complexity. Simulation and experimental results show that the algorithm can accurately and efficiently identify cohesion and internal friction angle for various soil types.

II. TERRAIN PARAMETER IDENTIFICATION

The parameter identification algorithm estimates the terrain cohesion c and internal friction angle ϕ online, using on-board rover sensors. These parameters can be used to compute the maximum terrain shear strength $\tau_{\max}$ from Coulomb's equation

$$\tau_{\max} = c + \sigma_{\max} \tan \phi \tag{1}$$

where $\sigma_{\max}$ is the maximum normal stress acting on a terrain region. Since soil failure occurs when the maximum shear strength is exceeded, knowledge of c and ϕ can be used to predict rover traversability on flat and sloped terrain. The parameters c and ϕ are also important scientific parameters for characterizing soils.

Here, the case of a rigid wheel traveling through deformable terrain is considered, since this is the expected condition for planetary exploration vehicles. This method also applied to terrestrial vehicles with pneumatic tires, if the inflation pressure is high compared to the terrain stiffness [5]. The following analysis assumes a smooth wheel but can also be applied to grousered wheels, since properly designed grousers can be modeled as an increased effective wheel radius [6].

To estimate terrain parameters, equations relating the parameters of interest to physically measurable quantities must be developed. A free-body diagram of a driven rigid wheel of radius r and width b traveling through deformable terrain is shown in Fig. 1. A vertical load W and a horizontal force DP are applied to the wheel by the vehicle suspension. A torque T is applied at the wheel rotation axis by an actuator. The wheel has angular velocity ω, and the wheel center has linear velocity V. The angle from the vertical at which the wheel first makes contact with the terrain is denoted θ_1. The angle from the vertical at which

the wheel loses contact with the terrain is denoted θ_2. Thus, the entire angular wheel–terrain contact region is defined by $\theta_1 + \theta_2$.

A stress region is created at the wheel–terrain interface, as indicated by the regions σ_1 and σ_2. Here σ_1 is the interface section from initial terrain contact (i.e., θ_1) to the point of maximum stress (i.e., θ_m), and σ_2 is the region from the point of maximum stress to final terrain contact (i.e., θ_2). At a given point on the interface, the stress can be decomposed into a component acting normal to the wheel at the wheel–terrain contact point σ and a component acting tangential to the wheel at the wheel–terrain contact point τ. The angle from the vertical at which the maximum stress occurs is denoted θ_m.

In the following analysis, it is assumed that the following quantities are known: the vertical load W, torque T, sinkage z, wheel angular speed ω, and wheel linear speed V. Issues related to sensing are discussed later in this paper.

Force balance equations for the system in Fig. 1 can be written as

$$W = rb \left(\int_{\theta_1}^{\theta_2} \sigma(\theta) \cos \theta \cdot d\theta + \int_{\theta_1}^{\theta_2} \tau(\theta) \sin \theta \cdot d\theta \right) \tag{2}$$

$$DP = rb \left(\int_{\theta_1}^{\theta_2} \tau(\theta) \cos \theta \cdot d\theta - \int_{\theta_1}^{\theta_2} \sigma(\theta) \sin \theta \cdot d\theta \right) \tag{3}$$

$$T = r^2 b \int_{\theta_1}^{\theta_2} \tau(\theta) \cdot d\theta. \tag{4}$$

The shear stress can be computed as

$$\tau(\theta) = (c + \sigma(\theta) \tan \phi) \left(1 - e^{\frac{r}{k}[\theta_1 - \theta - (1-i)(\sin \theta_1 - \sin \theta)]} \right) \tag{5}$$

where k is the shear deformation modulus, r is the wheel radius, and i is the wheel slip, defined as $i = 1 - (V/r\omega)$ [17].

The normal stress at the wheel-terrain interface is given by

$$\sigma(z) = \left(\frac{k_c}{b} + k_\phi \right) z^n \tag{6}$$

where b is the wheel width, k_c and k_ϕ are pressure-sinkage moduli, and n is the sinkage exponent [5]. This equation can be expressed as a function of the wheel angular location θ by noting that sinkage is related to θ as

$$z(\theta) = r(\cos \theta - \cos \theta_1). \tag{7}$$

Substituting (7) into (6) yields expressions for the normal stress distribution along the wheel–terrain interface as follows:

$$\sigma_1(\theta) = \left(\frac{k_c}{b} + k_\phi \right) (r(\cos \theta - \cos \theta_1))^n \tag{8}$$

$$\sigma_2(\theta) = \left(\frac{k_c}{b} + k_\phi \right)$$
$$\times \left(r \left(\cos \left(\theta_1 - \theta \frac{(\theta_1 - \theta_m)}{\theta_m} \right) - \cos \theta_1 \right) \right)^n. \tag{9}$$

To develop a parameter estimation algorithm, analytical expressions for the force balance (2)–(4) are required, since these equations relate physically measurable quantities (W, T, z, ω, V) to the parameters of interest (c, ϕ). However, (2)–(4) are not amenable to closed-form integration due to their complexity. This motivates the use of an approximate form of the stress [see (5), (8), and (9)].

A. Equation Simplification

Fig. 2 shows typical simulated plots of shear and normal stress distributions (as defined by (5), (8), and (9), respectively) around the rim
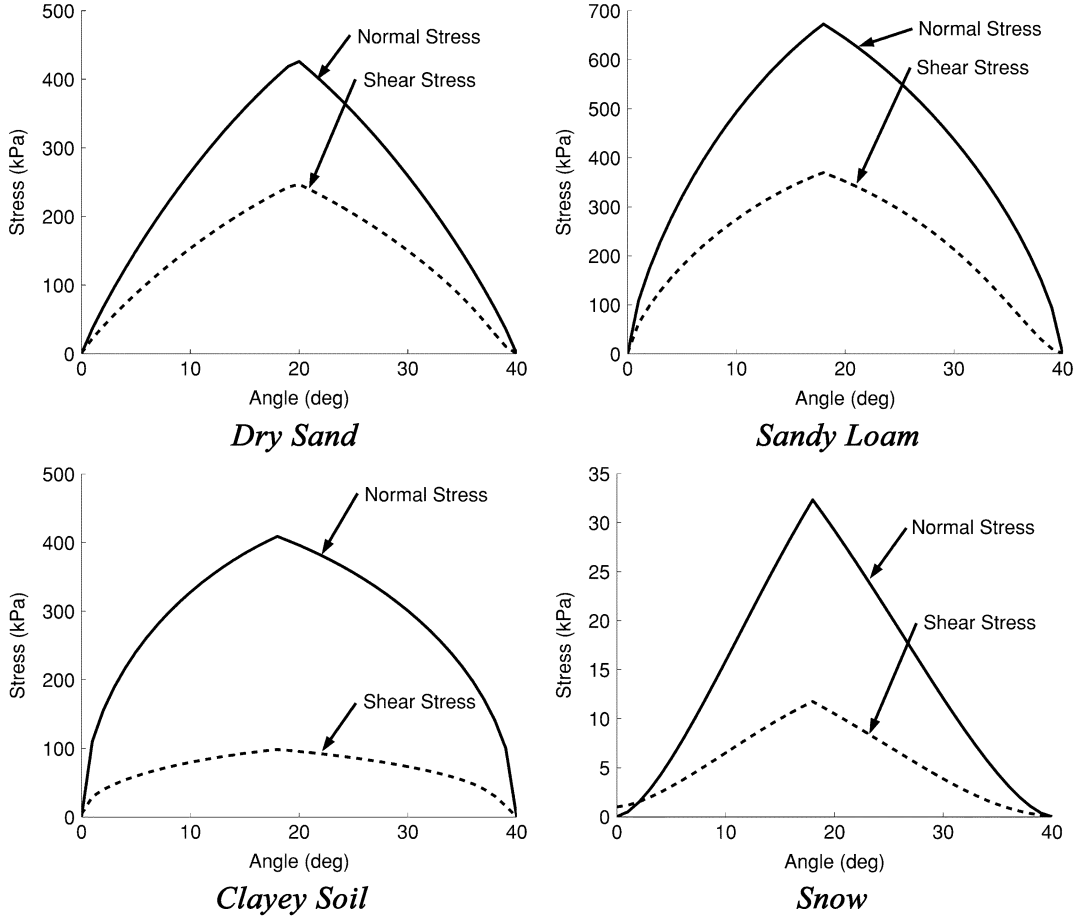
Fig. 2. Normal and shear stress distribution for various terrain types at moderate wheel slip.

TABLE I
PARAMETERS FOR VARIOUS TERRAIN TYPES

	Dry sand	Sandy loam	Clayey soil	Snow
n	1.1	0.7	0.5	1.6
c (kPa)	1.0	1.7	4.14	1.0
ϕ (deg)	30.0	29.0	13.0	19.7
k_c (kPa/m^{n-1})	0.9	5.3	13.2	4.4
k_ϕ (kPa/m^n)	1523.4	1515.0	692.2	196.7
k (m)	0.025	0.025	0.01	0.04

of a driven rigid wheel on various terrains at moderate wheel slip. Parameters used in these plots are listed in Table I and represent a diverse range of terrain types: dry sand, sandy loam, clayey soil, and snow [7], [17]. Fig. 2 shows that the shear and normal stress distribution curves are approximately linear for a diverse range of terrains.

Based on this observation, linear approximations of the shear and normal stress equations can be written as:

$$\sigma_1^L(\theta) = \frac{\theta_1 - \theta}{\theta_1 - \theta_m} \sigma_m \qquad (10)$$

$$\sigma_2^L(\theta) = \frac{\theta}{\theta_m} \sigma_m \qquad (11)$$

$$\tau_1^L(\theta) = \frac{\theta_1 - \theta}{\theta_1 - \theta_m} \tau_m \qquad (12)$$

$$\tau_2^L(\theta) = c + \frac{\theta}{\theta_m}(\tau_m - c) \qquad (13)$$

where σ_m and τ_m are the maximum values of the normal and shear stress, respectively. Equation (13) contains an offset term for cohesive soils.

Simplified forms of the force balance equations can be written by combining (2)–(4) with (10)–(13) (with $\theta_2 = 0$, since θ_2 is generally small in practice) to yield

$$W = rb \left(\int_0^{\theta_m} \sigma_2^L(\theta) \cos\theta \cdot d\theta + \int_{\theta_m}^{\theta_1} \sigma_1^L(\theta) \cos\theta \cdot d\theta \right.$$
$$\left. + \int_0^{\theta_m} \tau_2^L(\theta) \sin\theta \cdot d\theta + \int_{\theta_m}^{\theta_1} \tau_1^L(\theta) \sin\theta \cdot d\theta \right) \qquad (14)$$

$$\mathrm{DP} = rb \left(\int_0^{\theta_m} \tau_2^L(\theta) \cos\theta \cdot d\theta + \int_{\theta_m}^{\theta_1} \tau_1^L(\theta) \cos\theta \cdot d\theta \right.$$
$$\left. - \int_0^{\theta_m} \sigma_2^L(\theta) \sin\theta \cdot d\theta - \int_{\theta_m}^{\theta_1} \sigma_1^L(\theta) \sin\theta \cdot d\theta \right) \qquad (15)$$

$$T = r^2 b \left(\int_0^{\theta_m} \tau_2^L(\theta) \cdot d\theta + \int_{\theta_m}^{\theta_1} \tau_1^L(\theta) \cdot d\theta \right). \qquad (16)$$

Evaluation of (14) and (16) yields the following expressions for the normal load and torque:

$$W = \frac{rb}{\theta_m(\theta_1 - \theta_m)} \left[\sigma_m(-\theta_m \cos\theta_1 + \theta_1 \cos\theta_m - \theta_1) \right.$$
$$- \tau_m(\theta_m \sin\theta_1 - \theta_1 \sin\theta_m)$$
$$\left. - c\left(\theta_1 \sin\theta_m - \theta_m \sin\theta_m - \theta_m\theta_1 + \theta_m^2\right) \right] \qquad (17)$$

$$T = \frac{r^2 b}{2}(\tau_m\theta_1 + c\theta_m). \qquad (18)$$

TABLE II
PARAMETER SPACE FOR ALGORITHM ANALYSIS

Minimum value	Parameter	Maximum value
0.5	n	1.2
20.0	ϕ (deg)	40.0
0.0	c (kPa)	10.0
10.0	k_c (kPa/m^{n-1})	100.0
1000.0	k_ϕ (kPa/m^n)	5000.0
0.01	k (m)	0.03

Two assumptions are made in solving (17) and (18) for c and ϕ. The first is that the location of the maximum shear and normal stress occurs at the same location, θ_m. Analysis and simulation have shown that this assumption is reasonable for a wide range of soil types. With this assumption, an additional relation can be written, based on (5), as

$$\tau_m = (c + \sigma_m \tan \phi) \left(1 - e^{-\frac{r}{k}[\theta_1 - \theta_m - (1-i)(\sin \theta_1 - \sin \theta_m)]} \right). \quad (19)$$

The second assumption is that the angular location of maximum stress, θ_m, occurs midway between θ_1 and θ_2, i.e.,

$$\theta_m = \frac{\theta_1 + \theta_2}{2}. \quad (20)$$

This assumption is reasonable for a wide range of soils at moderate slip ratios [18]. This can be justified by noting that θ_m can be estimated from the relation $\theta_m = (c_1 + ic_2)\theta_1$, where c_1 and c_2 are terrain parameters. The range of c_1 and c_2 is generally $c_1 \approx 0.4$ and $0 \leq c_2 \leq 0.3$ [19]. Thus, for a wide range of slip ratios, θ_m will be near 0.5.

The system of (17)–(19) can be combined into a single equation relating cohesion and internal friction angle as follows:

$$c = \frac{\kappa_1 \tan \phi + \kappa_2}{\kappa_3 \tan \phi + \kappa_4} \quad (21)$$

where

$$\kappa_1 = A \left(\theta_1^2 W r + 4T \sin \theta_1 - 8T \sin \frac{\theta_1}{2} \right)$$

$$\kappa_2 = 4T \left(\cos \theta_1 - 2 \cos \frac{\theta_1}{2} + 1 \right)$$

$$\kappa_3 = A\theta_1 r^2 b \left(\sin \theta_1 - 4 \sin \frac{\theta_1}{2} + \theta_1 \right)$$

$$\kappa_4 = \theta_1 r^2 b \left(\cos \theta_1 - 2 \cos \frac{\theta_1}{2} + 2A \cos \theta_1 \right.$$
$$\left. - 4A \cos \frac{\theta_1}{2} + 2A + 1 \right)$$

$$A = 1 - e^{\frac{r}{k}[\frac{\theta_1}{2} + (1-i)(-\sin \theta_1 + \sin(\frac{\theta_1}{2}))]}.$$

Equation (21) can be rearranged to

$$\frac{\kappa_2}{\kappa_4} = \frac{\kappa_3}{\kappa_4} c \tan \phi + c - \frac{\kappa_1}{\kappa_4} \tan \phi. \quad (22)$$

The relative contribution of each term in the right-hand side of (22) was studied numerically over the range of parameters in Table II. This space encompasses a broad variety of terrain types. The simulated wheel radius r was 0.1 m, and the wheel width b was 0.1 m.

It was found that the maximum relative contribution of the $(\kappa_3/\kappa_4)c \tan \phi$ term was 2.47%. The other two terms had a significantly higher contribution [18]. Thus the $(\kappa_3/\kappa_4)c \tan \phi$ term is negligible, and (22) can be reduced to

$$\frac{\kappa_2}{\kappa_4} = c - \frac{\kappa_1}{\kappa_4} \tan \phi. \quad (23)$$

Equation (23) is a single equation in two unknowns. At least two unique instances of (23) are required to compute c and ϕ. During the parameter estimation process, it is expected that sensor data would be sampled at a frequency of several hertz. For each unique sensor sampling occurrence j, a unique instance of (23) can be written as

$$\frac{\kappa_2^1}{\kappa_4^1} = c - \frac{\kappa_1^1}{\kappa_4^1} \tan \phi$$

$$\vdots \qquad \vdots$$

$$\frac{\kappa_2^j}{\kappa_4^j} = c - \frac{\kappa_1^j}{\kappa_4^j} \tan \phi \quad (24)$$

or, in matrix form, as

$$\mathbf{K}_1 = \mathbf{K}_2 \begin{bmatrix} c \\ \tan \phi \end{bmatrix} \quad (25)$$

with

$$\mathbf{K}_1 = \begin{bmatrix} \kappa_2^1 / \kappa_4^1 & \cdots & \kappa_2^j / \kappa_4^j \end{bmatrix}^T$$

$$\mathbf{K}_2 = \begin{bmatrix} 1 & \cdots & 1 \\ -\kappa_1^1 / \kappa_4^1 & \cdots & -\kappa_1^j / \kappa_4^j \end{bmatrix}^T.$$

In practice, more than two equations are used to form an estimate of c and ϕ to decrease sensitivity to sensor noise. In this case, $\mathbf{K}_2$ is nonsquare and (25) can be solved in a least-squares sense, using the pseudoinverse of $\mathbf{K}_2$ as follows:

$$\begin{bmatrix} c \\ \tan \phi \end{bmatrix} = \left(\mathbf{K}_2^T \mathbf{K}_2 \right)^{-1} \mathbf{K}_2^T \mathbf{K}_1. \quad (26)$$

Note that singularity of $(\mathbf{K}_2^T \mathbf{K}_2)^{-1}$ only occurs in the degenerate case where nonunique sensor data are sampled (such as on perfectly flat terrain). This case will be discussed later.

All quantities in (26) can be sensed except the shear deformation modulus k (in the matrices $\mathbf{K}_1$ and $\mathbf{K}_2$). In practice, the estimation algorithm exhibits low sensitivity to k, particularly for large wheel radii and high slip ratios. Thus, k is chosen as a representative value for deformable terrain.

B. Sensing and Implementation Issues

In the preceding analysis, it was assumed that the vertical load W, torque T, sinkage z, wheel angular speed ω, and wheel linear speed V could be measured or estimated. Here, methods for measuring or estimating these inputs are discussed, along with other implementation issues for planetary rovers.

The vertical load W can be computed from a quasi-static force analysis of the rover, with knowledge of the rover configuration and mass distribution. Quasi-static analysis is valid since dynamic effects are negligible at the low speeds of these vehicles (on the order of 10 cm/s) [3]. The torque T can be estimated from the current input to the motor and an empirically determined mapping from current to torque. In applications where large thermal variation is expected (such as Martian surface exploration), motor temperature can be included in this mapping [11]. Note that torque and vertical load could be directly measured if the wheel were instrumented with a multi-axis force sensor. However, this adds cost and complexity to the rover.

The sinkage z can be computed with vision-based techniques or by kinematic analysis of the rover suspension [20], [21]. The wheel angular speed ω can be measured with a tachometer. The wheel linear speed V can be computed using inertial measurement unit (IMU) measurements. However, at low speeds, IMU velocity measurements can be highly degraded by noise. In this case, visual odometry can give more accurate results [22].

The sensors described above (i.e., rover configuration sensors, motor current sensor, wheel tachometer, IMU, and vision system) would likely be part of a planetary exploration rover. Thus, all required inputs can be measured or estimated with on-board rover sensors.

An important implementation issue is minimizing sensor noise. Most rover sensors can be modeled as a "true" signal corrupted by white noise. In this case, increasing the number of data points in (26) acts as an averaging filter and improves estimation accuracy. Other filtering techniques (such as the Kalman filter and its extensions) could also be applied to this problem.

Note that all data points used in a parameter estimate are assumed to be sampled from homogeneous terrain. For example, consider a rover moving at 5 cm/s with a sensor sampling rate of 5 Hz. If 10 data points are used to compute a parameter estimate, it must be assumed that the terrain is homogeneous within a 10-cm distance. If data are sampled from mixed or inhomogeneous terrain, resulting parameter estimates will be effective estimates of the combined terrain types. In general, assumptions regarding terrain homogeneity can be formed from *a priori* knowledge of local terrain characteristics. Terrain classification methods could also be used to detect changes in terrain type [23].

The final implementation issue arises for a rover traveling at constant velocity on flat terrain, where the matrix $(\mathbf{K}_2^T \mathbf{K}_2)^{-1}$ in (26) may be poorly conditioned. This occurs because the rover is collecting an identical set of sensor readings at each sampling instance. The ridge regression technique can be used to solve (26) in cases where $(\mathbf{K}_2^T \mathbf{K}_2)^{-1}$ is poorly conditioned as follows:

$$\begin{bmatrix} c \\ \tan\phi \end{bmatrix} = \left(\mathbf{K}_2^T \mathbf{K}_2 + \delta\mathbf{I} \right)^{-1} \mathbf{K}_2^T \mathbf{K}_1 \qquad (27)$$

where δ is a small positive constant that can be optimized by techniques such as cross validation [24]. In practice (and in the results presented below), natural terrain variation will usually lead to acceptable equation conditioning. Deliberately inducing variable wheel slip also improves parameter estimates on flat terrain.

III. SIMULATION RESULTS

Simulations were conducted of a single driven wheel traveling through deformable terrain. The purpose was to examine algorithm accuracy under various terrain conditions. In all simulations, the wheel traveled at approximately 0.1 m/s. The wheel had radius 0.1 m, width 0.1 m, mass 10 kg, and inertia 0.05 kg·m^2. A proportional-derivative control algorithm commanded the wheel. The simulated sampling rate was 20 Hz. Further details of the simulation are given in [18].

Simulations were first performed with noise-free inputs W, T, z, and i to study fundamental algorithm accuracy. Random variation of 15% was introduced to W and i to simulate variation caused by uneven, natural terrain, where wheel load and velocity change as the rover configuration changes. During the estimation procedure, the shear deformation modulus k was assumed to be 150% of its actual value to study algorithm sensitivity to this parameter.

Estimates of cohesion and internal friction angle were computed for 15 625 evenly spaced parameter sets in the parameter space described in Table II. This parameter space represents a broad variety of terrain types. Five sampled data points were used to compute each parameter estimate.

The root mean square (rms) error between the estimated and actual c over all simulations was 0.21 kPa (c ranges from 0 to 10 kPa). The rms error between the estimated and actual ϕ over all simulations was 1.62° (ϕ ranges from 20° to–40°). This shows that the approximations introduced in Section II-A do not introduce significant error into the estimation algorithm. The computational load for the algorithm was approximately 1 ms per estimation cycle for unoptimized Matlab code on a 933-MHz desktop PC.
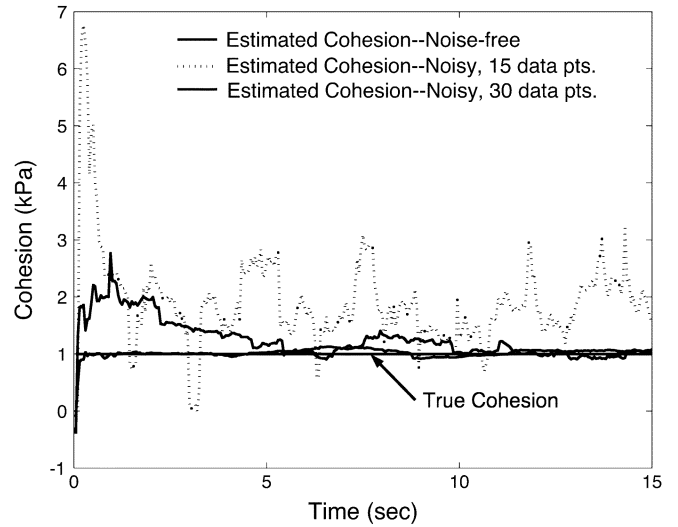

Fig. 3. Simulated estimation of cohesion of dry sand for a noise-free case, a noisy case using 15 data points, and a noisy case using 30 data points.

Simulations were then run to study the effect of sensor noise on estimation accuracy. The inputs W, T, z, and i were corrupted with white noise with standard deviation equal to 10% of their maximum value. Again, estimates of cohesion and internal friction angle were computed for the 15 625 parameter sets described above. The shear deformation modulus k was assumed to be 150% of its actual value, and ten sampled data points were used to compute each parameter estimate.

The rms error between the estimated and actual c over all simulations was 1.57 kPa. The rms error between the estimated and actual ϕ over all simulations was 4.12°. As expected, increasing the sensor noise levels leads to increased parameter estimation error. Simulations were then run with the number of sampled data points increased to 30. The rms error between the estimated and actual c was reduced to 0.63 kPa and for ϕ to 2.11°. The computational load for the algorithm was approximately 3 ms per estimation cycle. This suggests that it is possible to compute accurate parameter estimates despite sensor noise, with low computational cost. It also shows that increasing the number of sampled data points used to form a parameter estimate decreases the error caused by sensor noise.

Figs. 3 and 4 show representative parameter estimation simulation results for dry sand (see Table I). It can be seen that the estimated parameters c and ϕ rapidly approach their true values in the noise-free case. Sensor noise degrades the accuracy of the estimated parameters compared to the noise-free case. The effect of sensor noise is diminished by increasing the number of sampled data points from 15 to 30. In general, it is possible to obtain accurate parameter estimates using relatively few data samples despite sensor noise.

IV. EXPERIMENTAL RESULTS

Experiments were performed on a laboratory terrain characterization testbed, shown in Fig. 5. The testbed consists of a driven rigid wheel mounted on an undriven vertical axis. The wheel assembly is mounted to a driven horizontal carriage. By driving the wheel and carriage at different rates, variable slip ratios can be imposed. The vertical wheel load can be changed by adding weight to the vertical axis.

The testbed is instrumented with encoders to measure angular velocities of both the wheel and the carriage pulley. The carriage linear velocity is computed from the carriage pulley angular velocity. The vertical wheel sinkage is measured with a linear potentiometer. The wheel torque T is measured by a Cooper Instruments torque sensor.
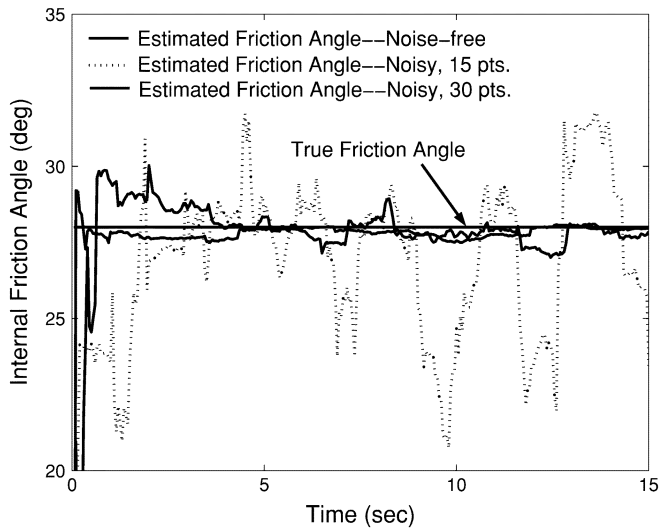
Fig. 4. Simulated estimation of internal friction angle of dry sand for a noise-free case, a noisy case using 15 data points, and a noisy case using 30 data points.
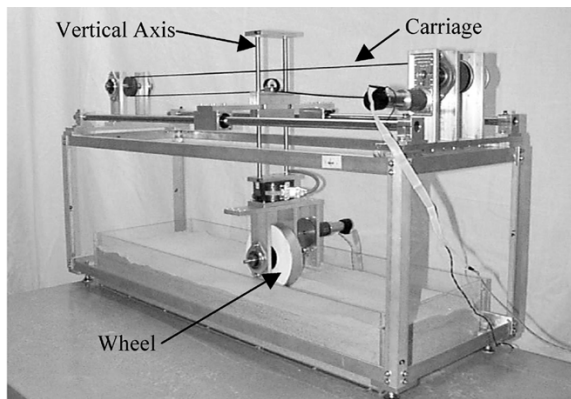

Fig. 5. Terrain characterization testbed.

The six-component wrench between the wheel and carriage is measured with a JR3 six-axis force/torque sensor. The force sensor allows measurement of the normal load W and drawbar pull DP. The testbed is controlled by a 133-MHz PC. The soil bin is 90 cm long, 30 cm wide, and 15 cm deep.

The wheel diameter and width are 14.6 and 6.0 cm, respectively. The wheel maximum angular velocity is 1.1 rad/s. This results in a maximum linear velocity of 8.0 cm/s. The wheel size and speed were chosen to be in the range of current and projected planetary rovers.

Three distinct soil types were chosen for experimentation: washed sand, dried bentonite clay, and compacted topsoil. Classical shear failure experiments were performed to determine c and ϕ for all soils. In these experiments, a vertical load is applied to homogeneous soil through a device called a bevameter, which is translated horizontally until shear failure occurs [5]. By varying the vertical load, a relationship between normal stress and shear stress can be observed. Numerous experiments were run to account for nonuniformity in soil mixing and moisture content. Table III summarizes the results of these experiments. These results agree with published values for similar soils [7], [17], [25]. A result of shear failure experiments for dried bentonite clay can be seen in Fig. 6. This figure shows a linear relationship between normal stress and shear stress, as predicted by (1).

TABLE III
RESULTS FROM SHEAR FAILURE EXPERIMENTS

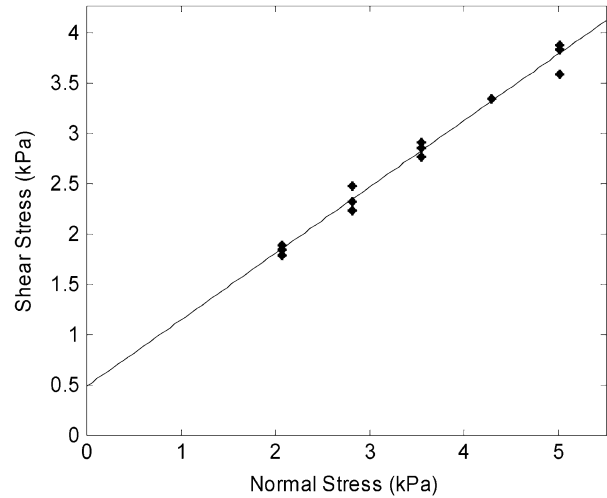|	c (kPa)	ϕ (deg)
Washed Sand	0.65 ± 0.24	32.1 ± 2.82
Dried Bentonite Clay	0.48 ± 0.19	33.7 ± 1.99
Compacted Topsoil	0.74 ± 0.24	44.3 ± 2.01

Fig. 6. Result from shear failure experiments for dried bentonite clay. Data points shown with best-fit line.
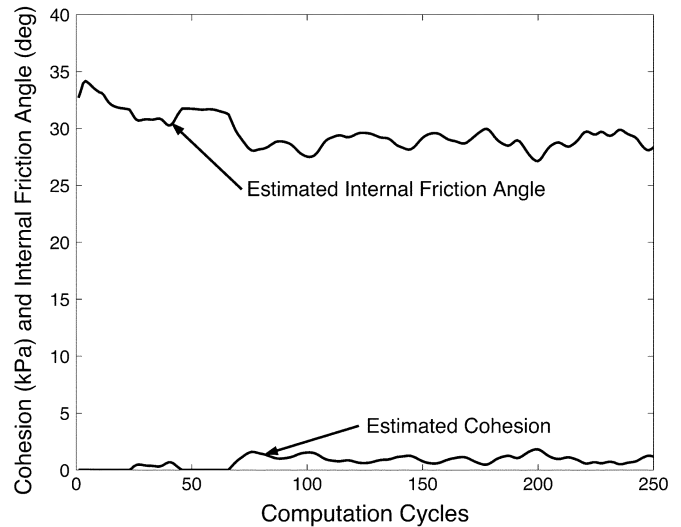

Fig. 7. Results of experimental estimation of cohesion and internal friction angle estimation for dried bentonite.

Parameter identification experiments were performed on each soil type. The shear deformation modulus k was assumed to be 0.05. Thirty sampled data points were used to compute each parameter estimate.

Fig. 7 shows the results of the estimation algorithm for dried bentonite. The estimated cohesion and internal friction angle rapidly converge to values of approximately 0.70 kPa and 32.1°, respectively. These values lie near or within the variance observed in the shear failure experiments.

Table IV summarizes the results of these experiments. Comparing these values with the values of Table III, it can be seen that the estimated values are similar to those measured via shear failure experiments. This suggests that the proposed approach can identify c and ϕ of various soils despite noisy sensors. Error and variation in estimated parameters

TABLE IV
RESULTS FROM TERRAIN PARAMETER ESTIMATION EXPERIMENTS

	c (kPa)	ϕ (deg)
Washed Sand	0.77 ± 0.48	29.6 ± 1.47
Dried Bentonite Clay	0.70 ± 0.35	32.1 ± 2.60
Compacted Topsoil	1.04 ± 0.43	43.7 ± 3.11

are likely due to nonuniformity in soil mixing and moisture content. Note that this variation is not unique to the proposed method, but is present in any soil property measurement technique. Estimation error is due to sensor noise and error in the assumed value of k. Also, at high slip ratios the testbed wheel exhibited control chatter, which degraded sensor readings.

These results show that the estimation algorithm produces reasonably accurate, online parameter estimates on an experimental system with noisy sensors, in a variety of terrain types. The level of accuracy shown by the algorithm would allow it to distinguish between distinct soil types such as crusty material or drift material. The computation time for each estimation cycle was approximately 1 ms on a 933-MHz desktop PC. Thus the approach is suitable for systems with limited on-board computation, such as planetary rovers.

V. SUMMARY AND CONCLUSION

An efficient online terrain parameter estimation algorithm has been presented. The estimation method is based on simplified forms of classical terramechanics equations. A linear least-squares estimator was used to estimate cohesion and internal friction angle in real time. Simulation and experimental results have shown that the method can estimate parameters of three different terrain types with good accuracy despite noise, using limited computation. This method could be used for planetary rovers for online terrain analysis.

ACKNOWLEDGMENT

REFERENCES

[1] S. Hayati, R. Volpe, P. Backes, J. Balaram, and W. Welch, "Microrover research for exploration of Mars," *Proc. AIAA Forum on Advanced Developments in Space Robotics*, 1996.

[2] P. Schenker *et al.*, "Lightweight rovers for Mars science exploration and sample return," in *Proc. SPIE XVI Intelligent Robots and Computer Vision Conf.*, vol. 3208, 1997, pp. 24–36.

[3] C. Weisbin, G. Rodriguez, P. Schenker, H. Das, S. Hayati, E. Baumgartner, M. Maimone, I. Nesnas, and R. Volpe, "Autonomous rover technology for Mars sample return," in *Proc. Int. Symp. Artificial Intelligence, Robotics, and Automation in Space*, 1999, pp. 1–10.

[4] R. Volpe, "Rover functional autonomy development for the Mars mobile science laboratory," in *Proc. IEEE Aerospace Conf.*, 2003, pp. 643–652.

[5] G. Bekker, *Theory of Land Locomotion*. Ann Arbor, MI: Univ. of Michigan Press, 1956.

[6] G. Bekker, *Introduction to Terrain-Vehicle Systems*. Ann Arbor, MI: Univ. of Michigan Press, 1969.

[7] J. Wong, *Theory of Ground Vehicles*. New York: Wiley, 1976.

[8] K. Iagnemma, H. Shibly, and S. Dubowsky, "On-line terrain parameter estimation for planetary rovers," in *Proc. IEEE Int. Conf. Robotics and Automation*, 2002, pp. 3142–3147.

[9] K. Iagnemma and S. Dubowsky, "Mobile robot rough-terrain control (RTC) for planetary exploration," in *Proc. 26th ASME Biennial Mechanisms and Robotics Conf., DETC 2000*, 2000.

[10] M. Moore, R. Hutton, R. Scott, C. Spitzer, and R. Shorthill, "Surface materials of the Viking landing sites, Mars," *J. Geophys. Res.*, vol. 82, no. 28, pp. 4497–4523, 1977.

[11] J. Matijevic *et al.*, "Characterization of Martian surface deposits by the Mars pathfinder rover, Sojourner," *Science*, vol. 278, no. 5, pp. 1765–1768, 1997.

[12] H. Moore, D. Bickler, J. Crisp, H. Eisen, J. Gensler, A. Haldemann, J. Matijevic, and L. Reid, "Soil-like deposits observed by Sojourner, the Pathfinder rover," *J. Geophys. Res.*, vol. 104, no. E4, pp. 8729–8746, 1999.

[13] Y. Nohse, K. Hashuguchi, M. Ueno, T. Shikanai, H. Izumi, and F. Koyama, "A measurement of basic mechanical quantities of off-the-road traveling performance," *J. Terramechan.*, vol. 28, no. 4, pp. 359–370, 1991.

[14] I. Shmulevich, D. Ronai, and D. Wolf, "A new field single wheel tester," *J. Terramechan.*, vol. 33, no. 3, pp. 133–141, 1996.

[15] G. Caurin and N. Tschichold-Gurman, "The development of a robot-terrain interaction system for walking machines," in *Proc. IEEE Int. Conf. Robotics and Automation*, vol. 2, 1994, pp. 1013–1018.

[16] A. Le, D. Rye, and H. Durrant-Whyte, "Estimation of track-soil interactions for autonomous tracked vehicles," in *Proc. IEEE Int. Conf. Robotics and Automation*, 1997, pp. 1388–1393.

[17] J. Wong, *Terramechanics and Off-Road Vehicles*. Amsterdam, The Netherlands: Elsevier, 1989.

[18] S. Kang, "Terrain parameter estimation and traversability assessment for mobile robots," M.S. thesis, Mass. Inst. Technol., Cambridge, 2003.

[19] J. Wong and A. Reece, "Prediction of rigid wheels performance based on analysis of soil-wheel stresses, part I," *J. Terramechan.*, vol. 4, no. 1, pp. 81–98, 1967.

[20] K. Iagnemma, S. Kang, C. Brooks, and S. Dubowsky, "Multi-sensor terrain estimation for planetary rovers," in *Proc. Symp. Artificial Intelligence, Robotics, and Automation in Space*, 2003.

[21] B. Wilcox, "Non-geometric hazard detection for a Mars microrover," in *Proc. AIAA Conf. Intelligent Robotics in Field, Factory, Service, and Space*, vol. 2, 1994, pp. 675–684.

[22] C. Olson, L. Matthies, M. Schoppers, and M. Maimone, "Stereo egomotion improvements for robust rover navigation," in *Proc. IEEE Int. Conf. Robotics and Automation*, 2001, pp. 1099–1104.

[23] P. Bellutta, R. Manduchi, L. Matthies, K. Owens, and A. Rankin, "Terrain perception for DEMO III," in *Proc. Intelligent Vehicle Symp.*, 2000, pp. 326–332.

[24] G. Golub and C. van Loan, *Matrix Computations*. Baltimore, MD: Johns Hopkins Univ. Press, 1996.

[25] R. Yong, E. Fattah, and N. Skiadas, *Vehicle Traction Mechanics*. Amsterdam, The Netherlands: Elsevier, 1984.